Report Number 10/58

Particle-scale structure in frozen colloidal suspensions from small angle X-ray scattering

by

Melissa Spannuth, S. G. J. Mochrie, S. S. L. Peppin, J. S. Wettlaufer

Oxford Centre for Collaborative Applied Mathematics
Mathematical Institute
24 - 29 St Giles'
Oxford
OX1 3LB
England

Particle-scale structure in frozen colloidal suspensions from small angle X-ray scattering

Melissa Spannuth*

Department of Geology and Geophysics, Yale University, New Haven, CT 06520, USA

S. G. J. Mochrie

Department of Physics, Yale University, New Haven, CT 06520, USA

S. S. L. Peppin

OCCAM, Mathematical Institute, University of Oxford, St. Giles Road, Oxford OX1 3LB, UK

J. S. Wettlaufer

Department of Geology and Geophysics, Yale University, New Haven, CT 06520, USA

Department of Physics, Yale University, New Haven, CT 06520, USA and

Program in Applied Mathematics, Yale University, New Haven, CT 06520, USA

(Dated: November 3, 2010)

Abstract

During directional solidification of the solvent in a colloidal suspension, the colloidal particles segregate from the growing solid, forming high-particle-density regions with structure on a hierarchy of length scales ranging from that of the particle-scale packing to the large-scale spacing between these regions. Previous work has mostly concentrated on the medium- to large-length scale structure, as it is the most accessible and thought to be more technologically relevant. However, the packing of the colloids at the particle-scale is an important component not only in theoretical descriptions of the segregation process, but also to the utility of freeze-cast materials for new applications. Here we present the results of experiments in which we investigated this structure across a wide range of length scales using a combination of small angle X-ray scattering and direct optical imaging. As expected, during freezing the particles were concentrated into regions between ice dendrites forming a microscopic pattern of high- and low-particle-density regions. X-ray scattering indicates that the particles in the high density regions were so closely packed as to be touching. However, the arrangement of the particles does not conform to that predicted by any standard inter-particle pair potentials, suggesting that the particle packing induced by freezing differs from that formed during equilibrium or steady-state densification processes.

PACS numbers: 82.70.Dd,64.75.Xc

* melissa.spannuth@gmail.com

Interest in directional solidification, or freeze-casting, of suspensions of particles has surged recently owing to the relative versatility, simplicity and cost-efficiency of the process for fabricating complex composite materials [1]. This method has been used to create materials for applications such as tissue scaffolds [2], biomimetic materials [3], photonic structures [4], and metal-matrix composites [5]. In addition, directional solidification has been shown to be effective for water purification [6] and occurs naturally when the ground freezes [7]. In all of these cases, the segregation of particles from the growing solid and the consequent increase of particle concentration in the fluid regions are paramount. In particular, the structure of the regions of segregated particles is important for performance of the material in many applications. This structure occurs on a variety of length scales from the relatively large scale of individual regions of segregated particles to the single particle scale of the packing density of segregated particles. Although most research has focused on the large-scale structure, the particle-scale structure is key to understanding the particle rejection behavior and hence predicting the large-scale structure.

In a very dilute suspension, rejection of single particles from a solidfication front is well understood as resulting from fluid flow into the premelted film that separates the particles from the growing solid (e.g., references [8–10]). In non-dilute suspensions, the same fundamental rejection mechanism is responsible for particle segregation during solidification, but the comprehensive interaction between the growing solid and the large number of particles found in non-dilute suspensions is not well understood. Conceptually, rejection increases the particle concentration in the fluid until the concentration reaches a threshold. Further particle rejection is untenable and the solidification front either becomes unstable or engulfs particles, or both [11]. The morphology of the instability or the mode of particle incorporation creates macro- and microscopic patterns of high- and low-particle-density regions. Depending upon the freezing conditions, commonly observed patterns include, among others, lamellae oriented parallel or perpendicular to the solidification direction, branching or hexagonal networks of nearly pure solid, and seemingly disordered crack-like patterns (e.g., references [11–17]). Similarities between these patterns and those formed during drying of colloidal suspensions (e.g., reference [18]) or jamming of suspensions flowing through constrictions (e.g., references [19, 20]) suggest that the physics underlying the colloid behavior may be similar as well, though the driving forces in each case differ. Thus, knowledge gained from studying structures in freezing colloidal suspensions may be applicable to dense

colloidal suspensions in diverse circumstances.

Presently, there is no theory that can fully predict the morphology or detailed characteristics of the patterns that form. However, a continuum approach analogous to that describing binary alloy solidification has been successful in predicting the transition from particle pushing to particle capture [11, 15, 16]. This description requires information about the particles near the freezing front, such as the packing density and rate of diffusion in the suspension. Although these quantities are modelled assuming that the particles behave as hard spheres, it is unknown whether this equilibrium approach to the statistical mechanics of the particles is accurate, or whether the forces associated with the solid growth and concomitant fluid flow affect the particle behavior. Furthermore, a hard sphere pair potential is not a good approximation of the inter-particle interactions for many systems of interest. Therefore, it is important to understand the particle-scale structure and behavior in solidifiying colloidal suspensions.

This type of information is difficult to obtain experimentally because the particle concentrations and materials typically involved make the suspensions opaque to visible light. In addition, the particles are often too small to observe individually and the structures that form are three-dimensional. As a result, most studies involve postmortem analysis of samples after sublimation of the solid and sintering or other fixing of the particle structure (e.g., references [2–4, 14, 21, 22]). As discussed in reference [23], this gives only a two-dimensional view of the three-dimensional structure, provides only static information about the final particle arrangement, and may be skewed by modification of the structure during sublimation and sintering.

A couple of experiments have overcome some of these difficulties by using either a very thin sample cell and transparent materials [24], or applying X-ray techniques (radiography and tomography) to thicker samples [23]. The thin sample chamber produces a quasi-two-dimensional system that can be observed with visible light microscopy for sufficiently low particle concentrations, while X-ray techniques can probe inside visibly opaque samples. X-ray tomography can even provide a full three-dimensional reconstruction of the samples. All allow samples to be viewed during the freezing process, though the long acquisition time for tomography allows only relatively slow solidification rates [16]. Improved X-ray tomography may relax this restriction [25]. Yet, none of these techniques provide information about the particle-scale structure of the samples. In order to obtain this information, we used small

angle X-ray scattering (SAXS), which provides a Fourier-space representation of the mass distribution within the samples on the scale of one to several times the particle radius.

Here we present the results of a joint X-ray scattering and direct imaging study. Our experiments benefit from the relative simplicity of a thin sample chamber, which allows sufficient light transmission to produce direct images of the samples. The images provide a basis for interpreting the SAXS intensity data collected before freezing, after melting, and while the samples were frozen. Most importantly, while frozen the data exhibit features related to the structure of the regions of segregated particles that formed during freezing. In particular, we find that the particles are very densely packed, even touching, and their arrangement does not conform to any predicted by standard models of inter-particle interactions. Therefore, the freezing process must cause particles to pack together in an unusual manner, possibly by creating inter-particle pressures that cannot be attained in the unfrozen solutions. This is an important point that must eventually be accounted for in solidification models, but more generally it raises questions about the arrangement of particles in dense suspensions under external forcing.

I. X-RAY SCATTERING BACKGROUND

As various light scattering techniques are commonly used to study a variety of materials, especially soft matter such as colloidal solutions, glasses or gels (e.g., references [26–28], the X-ray scattering methods used in this study may be familiar to many readers. However, in order to ensure that this paper is reasonably self-contained, we provide the necessary background in this section.

For optically opaque materials, X-ray scattering can provide information about the structure at length scales on the order of several to around 1000 nm depending on the scattering setup employed. The small angle X-ray scattering setup we used spans length scales from about 30 to 300 nm. SAXS probes variations in the density of electrons in a material (usually analogous to the mass density). In a colloidal suspension (fluid or frozen), the predominant density difference is between the colloidal particles and the solvent or its solid phase. Therefore, scattering occurs primarily from the particles and SAXS data reflect the density variations associated with the size of the colloidal particles and the predominant inter-particle spacings [29]. However, as in the X-ray Diffraction (XRD) techniques com-

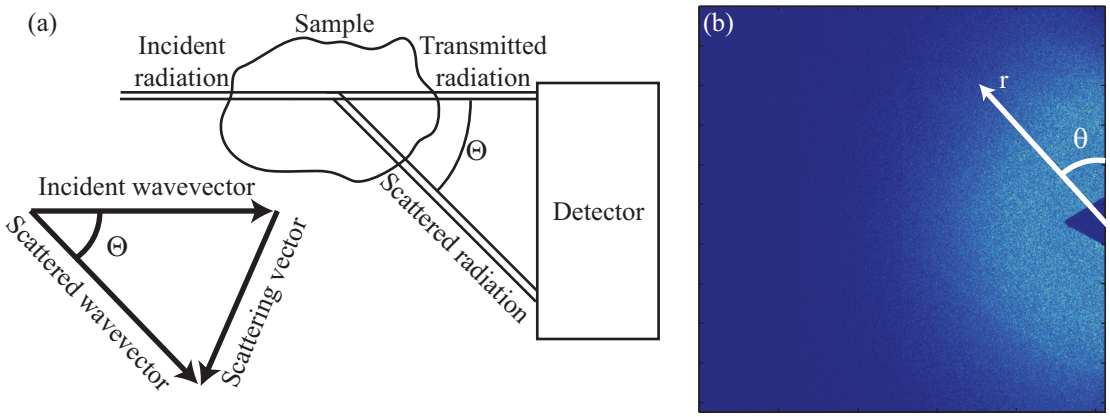

FIG. 1. (Color online) The schematic diagram in (a) shows a typical X-ray scattering experiment (not to scale) with the wavevectors of the incident and scattered radiation and the scattering vector labeled. The plot in (b) shows a false color image of the intensity $I(r,\theta)$ at each pixel on the detector. Cool colors indicate lower intensity and warm colors higher intensity. The dark blue triangle on the right hand side is the beam stop, which blocks the intense transmitted beam.

monly used in crystallography, these density variations are disclosed in reciprocal, or Fourier, space. Thus, SAXS is not generally a direct method and a model is needed to interpret the experimental results in terms of actual structure. At the most basic level, scattering vectors (or wavevectors) with higher scattered intensity indicate structure existing within the sample on length scales proportional to the inverse of those scattering vectors. In this way, SAXS provides structural information about complex materials.

A typical SAXS experiment is shown schematically in Fig. 1a. The X-rays are incident upon the sample, scatter in all directions, and a detector placed in the far-field collects the scattered light to form images of the scattered intensity I. The images provide $I(r,\theta)$, where (r,θ) defines the position of a pixel on the CCD detector. An example image is shown in Fig. 1b. Each position on the detector corresponds to a different scattering vector $\mathbf{q}$. As shown in Fig. 1a, the scattering vector is the vector difference between the wavevectors of the incident and the scattered X-rays. The magnitude of $\mathbf{q}$ is thus related to the angle between the incident and scattered radiation Θ by $q = 4\pi/\lambda \sin(\Theta/2)$, where λ is the wavelength of the X-rays. In terms of the pixel's position r on the detector, $q = 4\pi/\lambda \sin[\tan^{-1}(r/L)/2]$, where L is the distance between the sample and the detector [29].

Note that the scattering vector magnitudes are azimuthally symmetric in that all points

a given distance r from the origin have the same magnitude of their scattering vector regardless of the value of θ. Frequently in experiments on colloidal suspensions the scattering is expected to be isotropic, so analysis solely in terms of the magnitude of the scattering vector q is acceptable. For the present discussion, we assume that the scattering is isotropic, so only the magnitude of $\mathbf{q}$ is needed (except where noted). However, by convention we continue to refer to q as the scattering vector or q-vector even though only the magnitude is important.

The resulting intensity as a function of q for identical particles can be expressed as

$$I(q) = \Phi_i \, E_{det} \, \Delta\Omega \, A_{det} \, d \, Tr \, \phi \, V_{part} \, (\Delta\rho)^2 \, P(q) \, S(q) \tag{1}$$

where Φ_i is the incident X-ray flux, E_{det} is the detector efficiency, $\Delta\Omega$ is the solid angle subtended by the detector, A_{det} is the area of the detector, d is the sample thickness, Tr is the transmission coefficient, ϕ is the particle volume fraction, V_{part} is the volume of a single particle, $\Delta\rho$ is the electron density contrast between the particles and the solvent, $P(q)$ is the form factor, and $S(q)$ is the structure factor [29, 30]. The parameters Φ_i, E_{det}, $\Delta\Omega$, A_{det}, d, Tr, ϕ, V_{part}, and $\Delta\rho$ form a q-independent scaling coefficient, so all information about the sample structure is contained within $P(q)$ and $S(q)$.

The form factor $P(q)$ describes the scattering from particles of a given size and shape. It can be calculated based on the distribution of mass within the particles for a variety of shapes (reference [31] lists many examples). The structure factor $S(q)$ describes the scattering from spatial correlations among the particle positions [32]. It is the Fourier transform of the radial distribution function, which describes the probability of finding two particles separated by a given distance. Theoretical estimates of structure factors typically rely on radial distribution functions derived for a specified inter-particle interaction (usually pair potentials such as hard sphere, square well, or Coulomb). In addition to an assumed inter-particle interaction, a closure relation is needed to relate the inter-particle potential to the particle distribution. The different closure relations are more or less accurate depending upon the particle concentration and strength of interaction. Therefore, explicit expressions for $S(q)$ are only available for certain types of particles obeying particular interactions and under specific circumstances (reference [31] lists many examples). Nonetheless, this procedure produces accurate structure factors for many different systems, and fitting SAXS data to a model structure factor can provide information about the particle concentration

(number density or volume fraction) and the strength of inter-particle interactions.

For systems that do not permit the use of an a priori model or for which there are no models suggested by independent experimental results, SAXS data can still be considered in terms of the radial distribution function, though quantitative interpretation relies more upon the qualities of the scattered intensity as a Fourier transform. As such, peaks in SAXS data correspond to structures on length scales of roughly $2\pi/q_{peak}$ [29, 33]. However, it should be noted that because $I(q)$ is the Fourier transform of real-space structure, the scattering at a given q-vector is influenced by structures at all length scales [29]. The peak width is related to the variation of this length scale around the primary one. For example, a sharper peak means that the sample has a well-defined length scale, whereas a broader peak represents a broader distribution of length scales in the structure. Even when the intensity does not have a peak, enhanced scattering at a particular scattering vector indicates structure on the scale of $2\pi/q$ because the magnitude of the scattering at a particular length scale is proportional to the number of particles separated by that length. In terms of the particles' radial distribution function, the primary peak in $S(q)$ represents the average distance to a particle's nearest neighbors. The peak height is related to the average number of nearest neighbors (lower peak height corresponding to fewer neighbors). In this way, the location, width, and height of SAXS peaks as well as the magnitude of scattering away from the main peaks are related to the average particle separation, which reflects the particle concentration, and the amount of heterogeneity in the spatial distribution of the particles.

Thus, SAXS provides a way to probe the structure of complex, optically opaque materials. Changes in the location and shape of peaks in the scattering can provide information about the length scales of this structure, but obtaining quantitative measures of particle arrangement or concentration requires the use of an a priori model for the inter-particle interactions.

II. MATERIALS AND METHODS

For our X-ray scattering experiments, we used solutions of colloidal silica spheres dispersed in deionized water contained within a specially-designed thin, transparent sample chamber. The choice of materials and the experimental setup were each tailored to the specific requirements of the X-ray scattering experiment. This section provides the details

of the samples, sample cell, and other aspects of the procedures used in the experiments.

A. Materials

Our samples consisted of colloidal silica spheres (Bangs Labs) with radii of about 32 nm and polydispersity of about 18%, as determined from scanning electron micrographs and SAXS data (discussed below). The micrographs also showed that the particles were not perfectly spherical. The particles were stabilized against aggregation by surface-induced ionization. Silica is a good material for X-ray scattering because it has a large density contrast with water and ice (silica density is 1.96 g/cm^3 as reported by the manufacturer), which leads to a high scattered intensity. Using nearly spherical particles simplifies the interpretation of the scattering data because analytic expressions for the form factor exist for spheres. The size of the particles ensures that we can investigate particle-scale structure given the q range accessible in our X-ray scattering experiments.

We modified the as-received solutions by centrifuging to sediment the particles and then replacing the supernatant with deionized water (Fisher Scientific deionized, ultrafiltered; resistivity 0.5 MΩ/cm) in order to remove as much as possible of the ionic species (NaOH) added as a stabilizer by the manufacturer. Removal of the dissolved ions is important because they complicate interpretation of the experiments by affecting the stability of the solidification front [34], depressing the melting temperature of the solution [7], and congregating in large melt pockets long before bulk melting occurs [35]. Although removing the dissolved ions could destabilize the colloids and lead to aggregation, we did not observe any indications of this prior to freezing the solutions. In fact, the SAXS data from unfrozen solutions indicates that the final ion concentration is approximately 6 mM and the Debye length roughly 4 nm (see discussion below and reference [35]).

During centrifuging, we also adjusted the particle volume fraction of the solutions to $\phi_{HS} \approx 0.07$–0.08, where ϕ_{HS} is the volume fraction of equivalent hard spheres. This was estimated from the manufacturer's stated volume fraction and the amount of solvent removed, and was verified by the SAXS data assuming hard sphere interactions (discussed below). The actual particle volume fraction based on the physical particle radius was $\phi \approx 0.02$. The choice of volume fraction ensures strong scattering, while still allowing the samples to easily flow into the sample chamber.

B. Sample Cell

The sample chamber within the cell was formed by sandwiching an approximately 400 μm thick aluminum washer between two copper blocks. Circular pieces of thin polyimide film (Kapton) were epoxied across circular holes on each block to form the viewing area (Fig. 2). A thermoelectric cooling device (TEC, or Peltier cooler) in contact with the copper blocks controlled their temperature. A second TEC controlled the temperature of a copper arm (the "cold finger") that made thermal contact with the sample through physical contact with the outside of one of the windows. The cold finger had a cylindrical tip with inner diameter 2 mm and outer diameter 4 mm. By maintaining the temperature of the blocks above 0°C while that of the cold finger was lowered below 0°C, we created a nearly isothermal region within the cold finger inner diameter and a temperature gradient region between the cold finger outer diameter and the blocks. This allowed continuous contact with a reservoir of unfrozen solution, which helped alleviate pressure build-up during freezing and due to frost heaving when frozen [36]. The temperature control system and calibrated platinum resistance thermometric devices (Pt RTD's) provided ± 0.001°C precision and ± 0.05°C accuracy in temperature measurement, as well as temperature stability of ± 0.001°C over 10 minutes. Finally, the actual thickness of the sample chamber varied between about 200 μm and 400 μm due to the flexibility of the windows combined with manual positioning of the cold finger abutting one window.

C. Procedure

The X-ray scattering experiments were performed at beam line 8-ID of the Advanced Photon Source at Argonne National Laboratory. Details of the beam line are provided by references [37] and [38], but we will summarize the important aspects in this section along with the details of our particular experiment at this beam line.

For the X-ray experiments, the sample cell described above was placed in the beam line, which was evacuated to about 10^{-2} torr. Evacuating the beam line minimizes stray scattering of the X-ray beam from air or water vapor as it approaches the sample and then as the scattered X-rays travel to the detector. The fluid inside the sample chamber remained at atmospheric pressure because it was connected to the ambient atmosphere via the fill

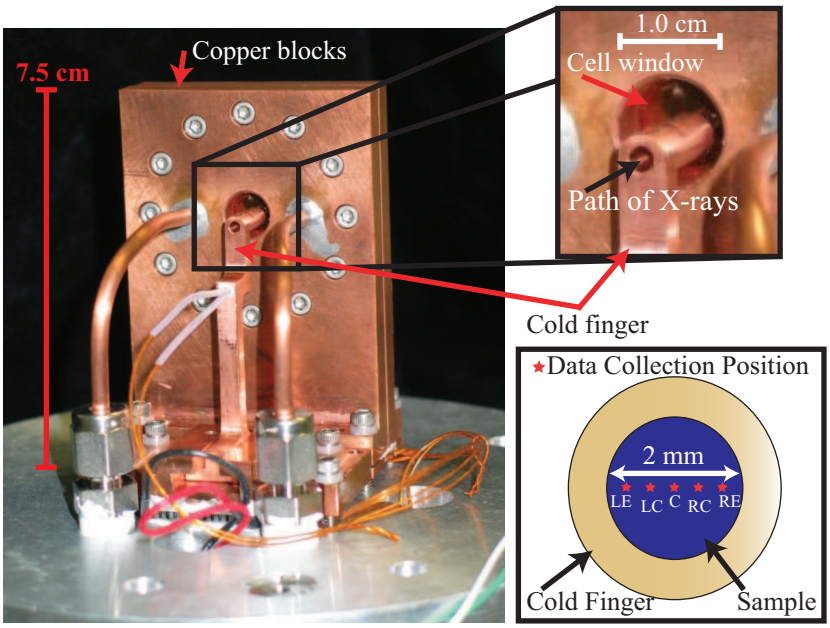

FIG. 2. (Color online) The image on the left shows the entire sample cell with the sample chamber and cold finger tip enlarged in the top right hand corner. In the lower right hand corner, the schematic diagram shows a plan-view of the cold finger tip with the approximate locations of X-ray data collection (LE = left edge, LC = left center, C = center, RC = right center, and RE = right edge).

lines.

We froze the samples by lowering the cold finger temperature to around −30°C, while the temperature of the blocks was maintained at a constant 1°C throughout all experiments. The samples cooled at rates up to 1°C/s at higher temperatures and nearly 0.25°C/s at lower temperatures. Ice typically nucleated between −20°C and −30°C, manifested by a slight change in the rate of decrease of the temperature due to the release of latent heat. After freezing, we studied the samples at temperatures between −2°C and 0°C at intervals as small as 0.05°C, always increasing the temperature as the sample age increased. Thus, temperature increased with time, though not continuously and not at precisely the same rate in all experiments.

We acquired X-ray scattering data at many temperatures before freezing, immediately after freezing, and as the temperature was increased towards 0°C. We could not acquire data during freezing due to the unpredictable timing of ice nucleation and the speed of ice

growth in the highly supercooled suspension. At each temperature, the X-ray beam was directed through the inner diameter of the cold finger and positioned at each of five different locations across this region as shown in Fig. 2. Thus, the X-ray experiments interrogated the isothermal region of the samples.

The X-rays we used had an energy of approximately 7.4 keV for a wavelength of about 0.17 nm. The beam cross-section was roughly $20\,\mu$m by $20\,\mu$m with a total incident flux of approximately 4×10^9 photons/s. For comparison, the cell thickness is several hundred μm and the particle size is only $0.032\,\mu$m, so there are many millions of particles in the scattering volume.

The scattered X-rays were collected by a charge-coupled device (CCD) camera, described in reference [38]. The CCD detector was exposed to scattered X-rays for 0.015 s per frame. To form a data set, a total of 500 frames were collected over about 110 s. During the readout time between frames and whenever data were not being acquired, the sample was blocked from X-ray illumination to limit radiation damage, which has been shown to induce melting [39].

Each frame in a particular data set was analyzed to create false color images of the scattered intensity like the example shown in Fig. 1b. Each image of scattered intensity was then divided into 100 concentric annular q-vector bins with the origin located at the center of the transmitted beam. These bins defined regions of the image with roughly equal scattering vector magnitude, but different scattering vector directions. We assumed that the scattering was isotropic, so the intensities from all pixels that fell into a particular bin were averaged (essentially an azimuthal average) and reported as the scattered intensity for a scattering vector with magnitude q equal to the average magnitude of all scattering vectors spanned by that bin. For each q, the azimuthally-averaged intensities from all frames in a given data set were further averaged to produce the intensity curve $I(q)$ given in equation 1. Finally, this curve was normalized by the incident flux, detector efficiency and area, and the solid angle spanned by the detector. We report the normalized intensity curve

$$I_N(q) = d\ Tr\,\phi\,V_{part}\ (\Delta\rho)^2\ P(q)\ S(q) \equiv A\,P(q)\ S(q) \tag{2}$$

in the results presented below. However, in what follows we will refer to this as simply $I(q)$. Generally, the intensity curve can also be normalized by the sample thickness and transmission coefficient to obtain the absolute scattered intensity, although we did not perform this

step because the sample thickness was not known precisely.

III. DIRECT IMAGING

Before delving into the SAXS results, we present direct images of freezing and frozen colloidal suspensions under conditions similar to those used in the X-ray scattering exepriments. These images provide a reference for interpreting the features in the SAXS intensity curves.

We used the same sample cell and type of colloidal solutions in the direct imaging experiments as in the SAXS experiments. In addition to colloidal samples, we also observed samples without particles, simply pure deionized water. The cell was situated between the light source and the camera, thus the samples were viewed in transmission. Images were focused onto a CCD detector (Unibrain Fire-i) with a 4x microscope objective lens resulting in an image scale of about 6 μm per pixel. In order to control condensation and obtain clear images, the cell and camera were housed inside a large, clear acrylic box that was constantly flushed with dry air and a chemical desiccant (W. A. Hammond Drierite Company) was also placed in the box. Temperature measurements in this setup had the same precision and accuracy as those in the X-ray scattering experiments, but the temperature was significantly less stable at ± 0.03°C over a period of about 10 s due to air currents from the dry air pumped into the box.

We froze the samples by lowering the temperature of the cold finger either directly with the TECs or with liquid nitrogen assisting the TECs. The samples typically froze at temperatures between -6°C and -20°C, though the freezing temperatures of individual samples had a high degree of uncertainty (up to ± 2°C). Thus, the water was supercooled when ice nucleated, resulting in two stages of ice growth: a rapid stage I with a cellular or dendritic morphology and a slower stage II with an apparently planar morphology.

During stage I, the low temperature of the sample caused rapid solidification and ice growth into a solution below the melting temperature T_m, leading to an unstable solidification front and a cellular or dendritic ice growth morphology [11, 16, 40, 41]. Figure 3 shows two sets of images obtained from movies of the sample freezing that illustrate this stage of ice growth in pure water (a) and a colloidal solution (b). The ice growth is cellular or dendritic with a linear pattern of alternating dark and light lines visible inside the cold

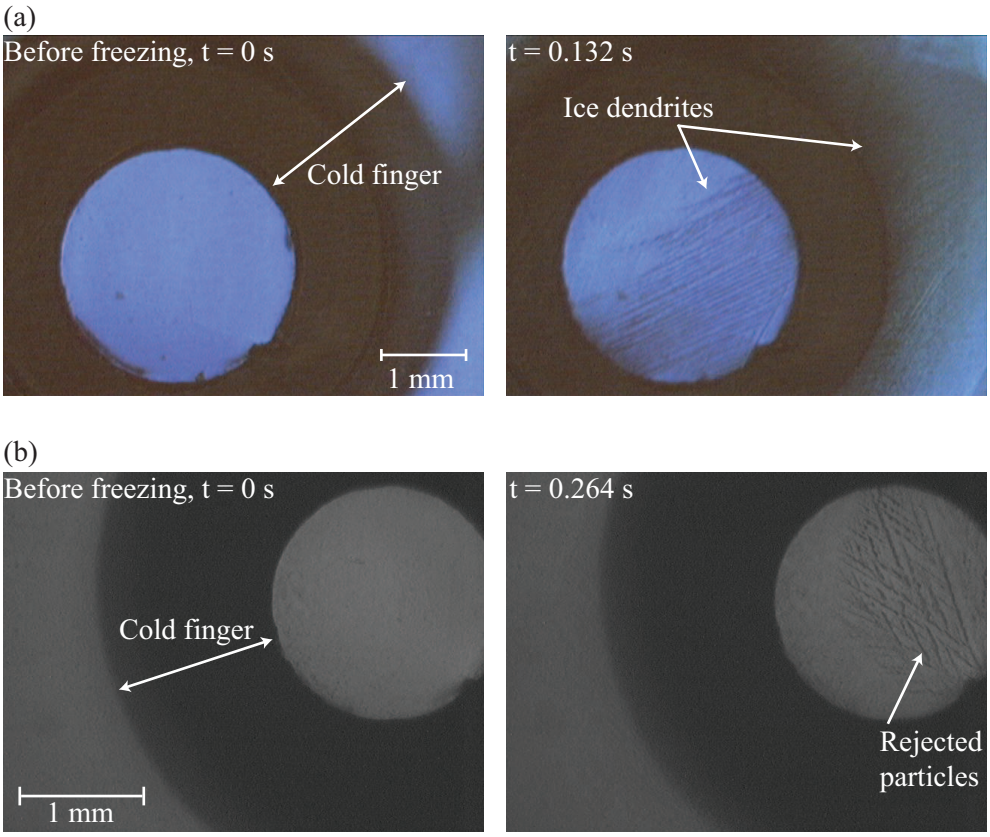

FIG. 3. (Color online) These images show two sets of before (time $t = 0$ s) and after ($t > 0$) snapshots from movies of stage I ice growth. The images in (a) show pure water, whereas those in (b) show a colloidal solution of silica spheres as described above, but with radius 142 nm. We note that we did not observe any significant differences in the direct imaging experiments between the behavior of solutions of these larger particles and solutions of the smaller particles (as used in the X-ray scattering). The samples in (a) were imaged through crossed polarizers, which highlights the ice against the optically isotropic water. Ice dendrites are visible in both sets: dark in (a) and light areas between dark regions of concentrated particles in (b).

finger in both samples. Because the entire field of view often froze in the time span of only a few frames (at frame rates of 7.5 or 15 fps), estimates of the freezing rates have large uncertainty. However, the values mostly fall between 10 mm/s and 40 mm/s, which agree fairly well with the morphology diagram for pure water in reference [41].

Stage I freezing ended when the entire sample had been warmed to T_m through release of latent heat of solidification. After this time, further freezing required further removal of heat

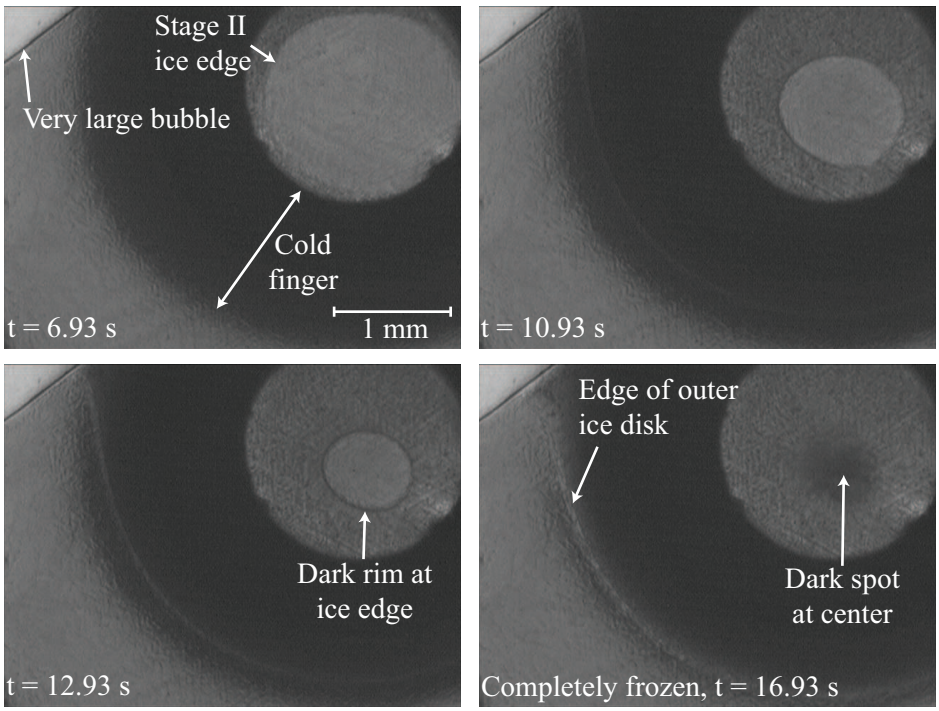

FIG. 4. These images show a sequence of snapshots of stage II solidification for a sample of 142 nm particles. In areas where stage II ice has formed the sample appears darker. The stage II ice edge is marked by a dark rim of particles being pushed ahead of the ice, which form a dark spot at the center upon complete solidification.

from the sample, which was effected by the TECs. We then observed an apparently planar ice front growing radially inwards and outwards from the cold finger, freezing any water that remained after stage I. Figure 4 contains a sequence of images showing this stage II ice growth. The ice edge moves radially inwards at a constant rate of 0.085 mm/s. Because the solidification rate during stage II is slower, measurements are much more accurate. All freezing rates are nearly constant throughout stage II ice growth and vary between about 0.1 mm/s and 1 mm/s among the samples. Although the stage II ice front appeared to be stable and planar, in fact it may have been unstable, just with a wavelength below the resolution of our imaging setup. Previous work [22] has shown that for solidification rates in the range of our experiments, the wavelength of the instability drops below 10 μm, which we would not be able to resolve.

During stage II, the linear pattern of light and dark stripes formed during stage I disappears from pure water samples, whereas it persists in colloidal samples. This pattern is

evident both in Fig. 4 and in the first image of the sequence in Fig. 5. Because the samples were viewed in transmission, areas of high particle density should appear dark whereas areas of low particle density should appear light. Therefore, we interpret the light and dark stripes present in colloidal samples as a pattern of high and low particle density imposed by the ice during freezing. In the pure water samples, they are simply an optical effect due to the edges of the dendrites, which disappear once the stage II ice growth has solidified all water remaining between the dendrites.

These observations indicate that the particles were rejected to the inter-dendrite regions during stage I and then engulfed by the ice during stage II. Comparing the freezing rates with the theoretical critical freezing rate for particle engulfment estimated by combining elements from references [10, 17, 42], we find that the particles should have been rejected from the growing ice during both stages [35]. Indeed, during stage I the particles were rejected into the inter-dendrite regions, and during stage II some of the particles not in the inter-dendrite regions were evidently rejected as dark patches appeared at the center of the cold finger in some samples. However, the particles rejected to the inter-dendrite regions were engulfed by stage II ice growth, perhaps by trapping between the dendrites [5, 16] or possibly due to their inclusion in large particle aggregates [35]. Thus, the process of freezing supercooled colloidal suspensions in our experimental setup results in a linear pattern of high- and low-particle-density regions due to the unstable freezing morphology.

The width of the stripes was typically tens of μm; for the sample shown in Fig. 5, initially the light (low density) regions were on average $17\,\mu$m across and the dark (high density) regions were on average $28\,\mu$m across. However, these patterns and the widths of the respective regions changed as the samples aged. We observed the evolution of the samples at different temperatures between -2°C and 0°C over time scales ranging from several hours up to one week. In general, the light areas became more rounded, and the linear dark features tended to merge with each other, their edges becoming simultaneously more sharply defined. Figure 5 contains a sequence of images illustrating this evolution. Our direct observations and dynamic X-ray scattering suggest that this evolution is driven by grain boundary motion due to coarsening of the polycrystalline ice in the samples [43].

Finally, upon melting, we observed that many dark objects up to $100\,\mu$m in size sedimented out of the solution. Presumably, these were aggregates of individual particles bound together during the freezing or aging process (images provided in reference [35]).

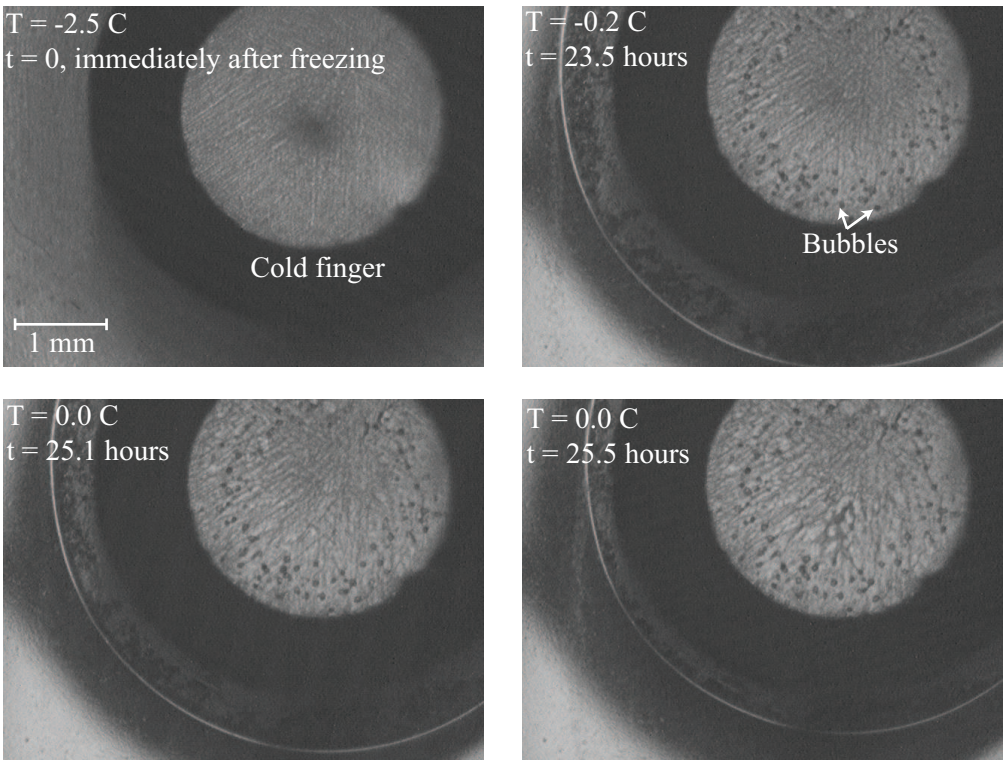

FIG. 5. These images show a sequence of snapshots of a frozen solution of 32 nm particles aging with the sample ages and temperatures indicated. The small dark spots near the cold finger are air bubbles. Because the water was not degassed before freezing, air gradually exolves from the ice.

In summary, the direct imaging experiments provide general information about the freezing process in our system. After deep supercooling, the initial stage of solidification is unstable with particles being rejected to the regions between ice dendrites to form a linear pattern of high and low particle density. During the second stage of solidification, this pattern is locked in as an apparently planar ice front grows across the cell. As the frozen samples evolve, the high-particle-density regions rearrange due to the motion of grain boundaries from ice crystal coarsening. These observations serve as a framework for understanding the results of the X-ray scattering experiments, which provide quantitative information about the particle-scale structure in these macroscopic features.

IV. SAXS RESULTS

The primary result of SAXS is the scattered intensity $I(q)$. Figure 6 shows typical examples of $I(q)$ for a sample before being frozen (circles) and when frozen (squares). The unfrozen data decrease smoothly as q increases, whereas the frozen data have two peaks: one at high q and another at low q, of which only the tail is visible. For all temperatures at which the sample was frozen, the intensity maintained the same general form with two peaks, though the position and width of the peaks changed. Upon melting, the scattered intensity reverted to the unfrozen form observed before the samples were frozen, though the details of the shape had changed. These data reflect the structural properties of the samples such as the particle size, shape, and inter-particle spacing. By fitting the intensities to a theoretical model (unfrozen data) and an empirical function (frozen data), we were able to quantify these structural properties and monitor how they evolved as the samples aged.

A. Unfrozen Intensity

For the unfrozen intensities, we obtained the particle size, polydispersity, and volume fraction by fitting the data to a function of the form $I(q) = A\,P(q)\;S(q)$ from equation 2, where A is a q-independent coefficient signifying the amplitude of the scattering, $P(q)$ is the particle form factor, and $S(q)$ is the structure factor. Though the particles are not perfectly spherical, we used a standard form factor for polydisperse spheres [44] that depends on the average particle radius R and the polydispersity parameter z:

$$P(q) = \frac{9z!\,(z+1)^6}{(qR)^6\,(z+6)!}\left[\frac{1}{2} + \frac{1}{2}\frac{z+2}{z+1}\,(qR)^2 + F^{(z+1)/2}U\right], \tag{3}$$

where

$$F = \frac{(z+1)^2}{(z+1)^2 + (2qR)^2},$$

$$U = -\frac{1}{2}\cos\left[(z+1)\,f\right] - qRF^{1/2}\sin\left[(z+2)\,f\right] + \frac{1}{2}\,(qR)^2\,\frac{z+2}{z+1}F\cos\left[(z+3)\,f\right],$$

and

$$f = \tan^{-1}\left[2qR/\,(z+1)\right].$$

This form factor is based on a Schulz-Zimm distribution of particle radii in which z describes the width of the distribution such that the mean squared deviation from R is $1/\,(z+1)$. For

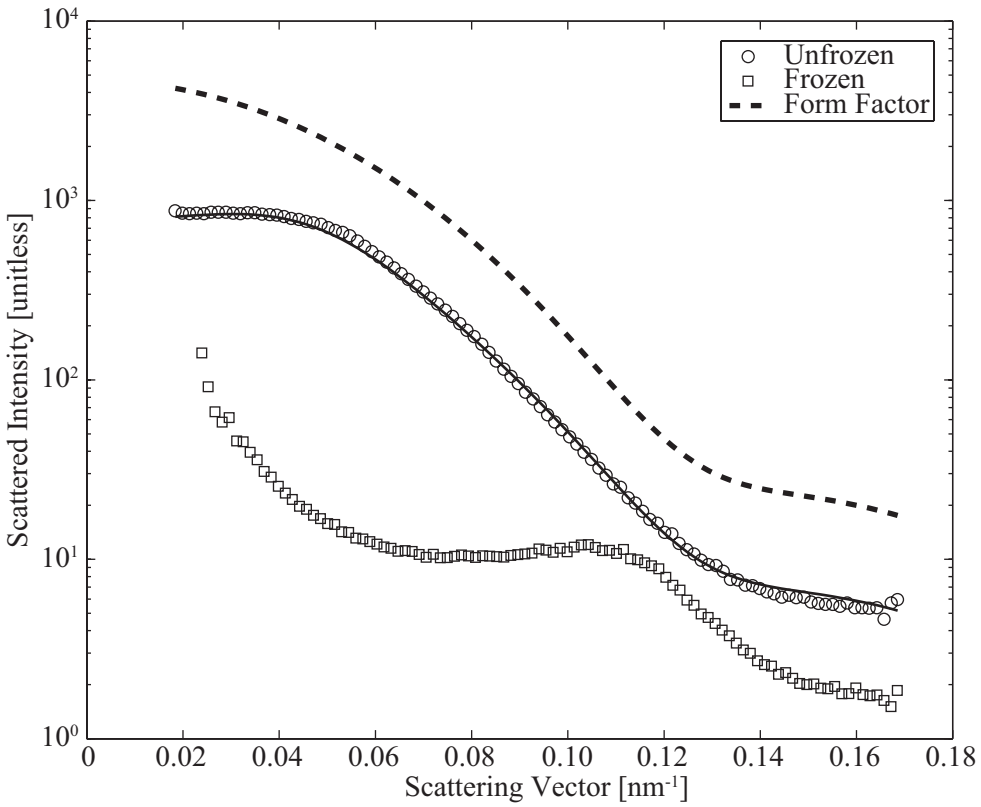

FIG. 6. SAXS intensity versus scattering vector taken at the center position from sample 2 before being frozen (circles) and at $T = -2.00°\mathrm{C}$ when frozen (squares). The solid curve represents the fit of the unfrozen data to a polydisperse sphere form factor and monodisperse hard sphere structure factor with $R = 32.4$ nm, $z = 31$, $A = 294$, $R_{HS} = 53.0$ nm, and $\phi_{HS} = 0.073$ as described in the text. For comparison, the dotted line shows only the form factor with the same parameters as above, but an arbitrary amplitude. For clarity the unfrozen data have been offset from the frozen data by multiplication with a constant coefficient.

the structure factor we used a function for monodisperse spheres of radius R_{HS} at volume fraction ϕ_{HS} interacting via a hard sphere potential [37]:

$$\begin{aligned} S(q) = \Big\{ 1 \; + \; & \tfrac{24\phi_{HS}}{u^3} \Big[a \left(\sin u - u \cos u \right) \\ & + \; b \left(\tfrac{2}{u^2-1} u \cos u + 2 \sin u - \tfrac{2}{u} \right) \\ & + \; \phi_{HS} \tfrac{a}{2} \left(\tfrac{24}{u^3} + 4 \left(1 - \tfrac{6}{u^2} \right) \sin u - \left(1 - \tfrac{12}{u^2} + \tfrac{24}{u^4} \right) u \cos u \right) \Big] \Big\}^{-1}, \end{aligned} \tag{4}$$

where

$$u = 2qR_{HS},$$

$$a = \frac{(1+2\phi_{HS})^2}{(1-\phi_{HS})^4},$$

and

$$b = -\frac{3}{2}\phi_{HS}\frac{(2+\phi_{HS})^2}{(1-\phi_{HS})^4}.$$

For each unfrozen data set, the fitting was performed using an iterative grid search method to find the parameters that minimized the mean squared residual. Due to the large range of intensity values, the logarithm of the data was used to determine the residuals. We also visually inspected each fit to ensure quality. The solid curve in Fig. 6 shows this fit to a typical data set.

Altogether there are five parameters in the fitting equations: the average particle radius R, the polydispersity z, the hard sphere radius R_{HS}, the hard sphere volume fraction ϕ_{HS}, and the scaling constant A. The average particle radius was 32 ± 1 nm and the polydispersity 29 ± 3 both before freezing and after melting, for a spread of about 18% around the average radius (as given above in section II A). The hard sphere radius was typically 53 ± 1 nm with the change between the pre-freezing and after-melting values negligible compared with uncertainty in the fitting. In contrast, the hard sphere volume fraction was typically between 0.07 and 0.09 before freezing, but usually dropped to between 0.03 and 0.07 after melting. We do not discuss A here because without measuring the absolute scattered intensity, changes in this parameter are difficult to interpret. Thus, most parameters did not change significantly from before freezing to after melting (to within the uncertainty in the fit), except that the hard sphere particle volume fraction decreased by a factor of 2 or more.

The average particle radius and the polydispersity reflect the actual physical extent of the particles. Thus, the near constancy of these parameters indicates that the physical size of individual particles and distribution of those sizes did not change during freezing or aging. The hard sphere radius, on the other hand, represents the effective radius of the particles in their interactions with each other (assuming they interact according to a hard sphere potential). Because R_{HS} is larger than R, the particles apparently *behaved* as if they were larger than their physical dimension. As a result, ϕ_{HS} overestimates the actual particle volume fraction ϕ. The two volume fractions can be related by $\phi = \phi_{HS}\,(R/R_{HS})^3$. This gives initial actual volume fractions of about 0.015 – 0.02 and final actual volume fractions between 0.007 and 0.015. As R_{HS} did not change significantly throughout the experiment, the decrease in ϕ_{HS} represents a real decrease in the bulk particle concentration from before

freezing to after melting.

B. Frozen Intensity

For the frozen data, we isolated the structure factor by dividing the intensities by the form factor given in equation 3 with $R = 32$ nm and $z = 29$. Because $I(q) = A\,P(q)\;S(q)$, dividing by $P(q)$ leaves a measured structure factor $S_m(q) = A\,S(q)$. Examples of $S_m(q)$ are shown in Fig. 7. Like the full intensity profile, the measured structure factor has a clear peak at high q-vectors and an upturn at low q-vectors. Whereas the upturn is more prominent in the full $I(q)$ because it is enhanced by the large values of $P(q)$ at low q (see dashed line in Fig. 6), conversely the peak is enhanced in $S_m(q)$. The upturn in the structure factor at low scattering vectors represents structure on length scales larger than several times the particle radius. The peak at higher scattering vectors reflects structure on the single particle length scale, giving information about the particles' nearest neighbors.

In order to obtain information about the particle packing, we attempted to fit our $S_m(q)$ with a variety of common structure factors with A as a free parameter. We were unable to obtain acceptable fits with structure factors derived from a hard sphere potential [37], sticky hard sphere (square well) potential [45, 46], or Coulomb repulsion [47]. Furthermore, we also attempted to modify the form factor by including a fractal cluster term [31] or a q^{-4} dependence [46], but neither improved the fits.

Instead, we fit the main, high q-vector peak with a Gaussian function given by

$$I(q) = \delta + A \exp\left[-\left(q - q_{peak}\right)^2 / \sigma^2\right], \tag{5}$$

where in δ is the q-independent offset, A is the q-independent peak height, q_{peak} is the peak location, and σ controls the peak width. In order to obtain reliable fits, we only used data between chosen low- and high-q-vector cutoffs. The low-q-vector cutoff was chosen as that scattering vector at which the measured structure factor reached its minimum value. The high-q-vector cutoff was defined as $q = 0.14$ nm^{-1}. We fit the plain values of $S_m(q)$ rather than their logarithm to emphasize fitting of the peak. The fitting was performed using an iterative grid search method to minimize residuals. As with the unfrozen data, we visually inspected the resulting fits to ensure good quality. The solid curves in Fig. 7 illustrate these fits.

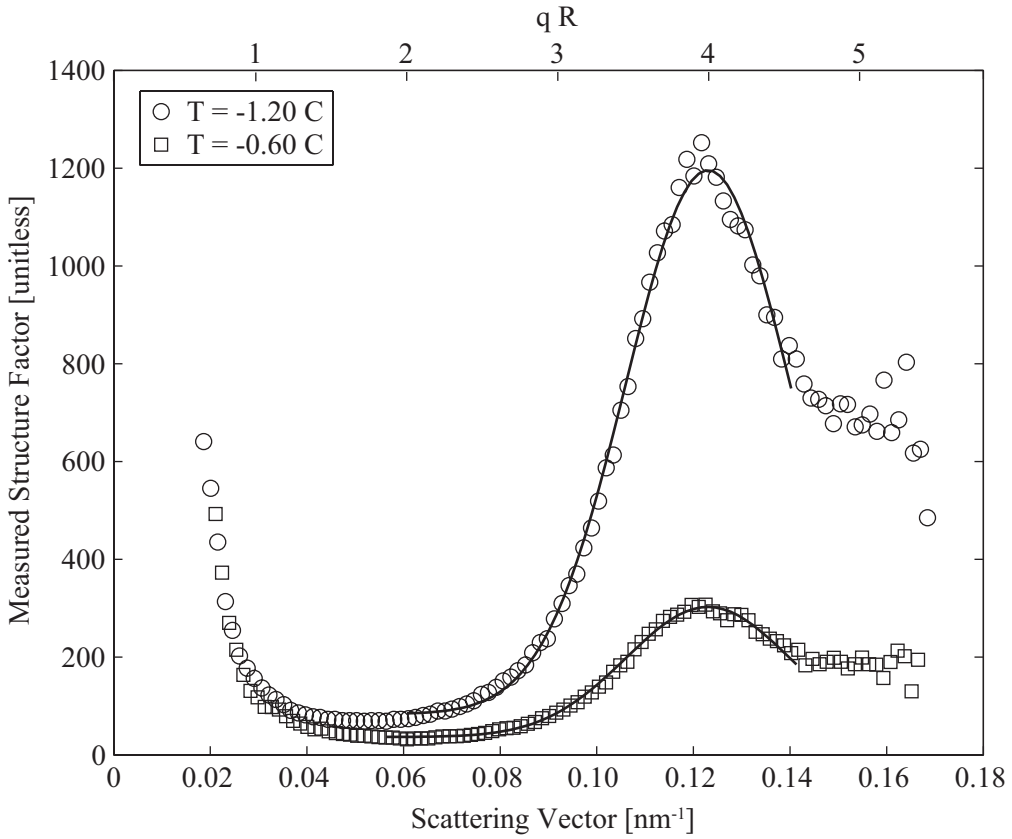

FIG. 7. Measured structure factors versus scattering vector taken at the left edge position from sample 5 at $T = -1.20°\text{C}$ (circles) and $T = -0.60°\text{C}$ (squares). Solid curves represent the Gaussian fits of the main peak as described in the text. Along the top of the plot, the horizontal axis is labeled in units of qR.

We performed this Gaussian fitting on all data sets for which the samples were frozen and examined the resulting fit parameters as a function of temperature (examples are shown in Fig. 8). We find that the peak position and peak width, which represent the predominant inter-particle spacing (nearest neighbor distance) and the distribution of inter-particle distances, are fairly constant at $q_{peak} \approx 0.123$ nm^{-1} ($q_{peak}R \approx 3.94$) and $\sigma \approx 0.017$ nm^{-1}, respectively, though the peak width appears to increase slightly in some cases. This indicates that the average inter-particle distance remained fairly constant as the samples aged. The increasing peak width indicates that the distribution of inter-particle distances widened slightly. The peak amplitude shows a very clear decreasing trend as the temperature increases, while the offset does not exhibit a clear trend. The offset is simply related to the

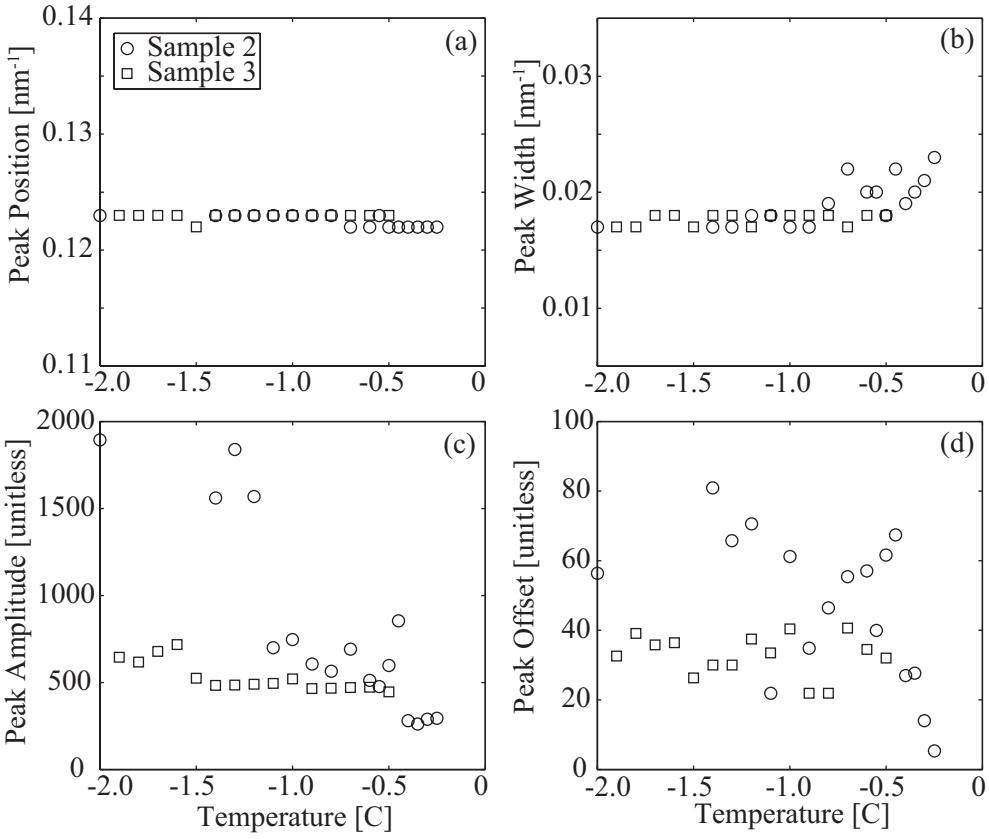

FIG. 8. Peak fit parameters versus temperature from the center position of two different samples (circles, sample 2; squares, sample 3). The peak position is in (a), the peak width is in (b), the peak amplitude is in (c), and the peak offset is in (d).

overall amount of scattering, which we expect to change between data sets as particles move into or out of the scattering volume. The decreasing peak amplitude indicates a decrease in the number of nearest neighbors. When combined with the increasing peak width, this suggests an increase in heterogenity of particle spacing as the temperature increased and the samples aged.

Altogether, SAXS reveals that the scattered intensity, and hence the sample structure, changed very dramatically when the samples froze and continued to evolve as the samples aged. The changes in $I(q)$ from before freezing to after melting indicate that the volume fraction of particles within the bulk solution decreased significantly. While the samples were frozen, the steady position of the high q-vector peak shows that the average nearest neighbor distance remained fairly constant. The slight widening of the peak and the decrease in its

amplitude suggest that the distribution of inter-particle distances widened and became more heterogeneous. In the next section, we interpret these results within the context of the direct images obtained from our laboratory experiments and with respect to established models for the structure factor.

V. DISCUSSION

These SAXS results provide quantitative information about the structures observed in the direct images, and conversely, the direct imaging experiments provide a framework for interpreting the SAXS results. In particular, direct observation revealed a linear pattern of high and low particle density that formed during the dendritic freezing of the colloidal solutions at high levels of supercooling. This pattern subsequently evolved as the samples aged, with regions of high density joining together and regions of low density enlarging. Furthermore, we observed particle aggregates sedimenting out of solution as the samples melted. Each of these observations can be identified with and quantified by features in the SAXS results.

For the following discussion it is important to note the relative size of the X-ray beam as compared with the pixel size in the direct images in order to maintain the proper perspective on the structures probed by the X-ray scattering. As the size of a single pixel in the direct imaging setup was approximately $6\,\mu$m square, the entire X-ray beam (approximately $20\,\mu$m square) covered roughly an equivalent area of 9 pixels (3 pixels by 3 pixels) in the direct images. Therefore, the scattering volume probed by the X-rays, and consequently the structures inferred from the scattering data, are comparable to the smallest details that could be resolved in the direct imaging experiments. However, this is still a large enough volume to contain many millions of particles ensuring a good statistical ensemble.

We first discuss the scattering data from unfrozen solutions. These data were fit to a model based upon polydisperse spherical particles that interacted as if they were monodisperse hard spheres. In fact, before being frozen the colloids likely interacted according to DLVO theory [48] because the attractive van der Waal's interaction at short range was counteracted by the long-range repulsive electrostatic interaction arising from surface-induced ionization. Generally, silica colloids have silanol (SiOH) surface groups which ionize in solution to form negatively charged SiO^- groups that give the particles an overall negative

charge and hence stabilize the solution [49]. The H^+ ions that dissociated from the surface mix with any other ions in the water and form a diffuse layer of higher ion concentration surrounding each of the particles – the diffuse electric double layer. The characteristic length scale for this layer is the Debye length and is related to the concentration of ions in the solvent [48]. Addition of other electrolytes to the solution also helps stablize the particles (e.g., the NaOH added by the manufacturer of our particles, which we attempted to remove). Thus, the particles were not actually hard spheres, although our SAXS data show that they could be accurately treated as such with an effective hard sphere radius somewhat greater than the actual particle radius. The effective hard sphere radius is larger than the actual radius due to the cloud of ions surrounding the particles; we can estimate the ionic strength of the solution from this hard sphere radius.

Several studies of colloids have found differences between the physical particle radius as measured by electron microscopy and the actual radius or effective hard sphere radius measured by static or dynamic light scattering [50–52], and indeed charge stabilized colloids have been found to behave as effective hard spheres [53]. However, the exact relationship between the effective hard sphere radius and the Debye length is not known. One estimate that was determined by theoretical and computational methods for the depletion interaction between two colloidal particles in a solution of macroions gives the effective hard sphere radius $R_{HS} = R + 5/\kappa$, where R is the actual particle radius and $1/\kappa$ is the Debye length. Using this formula, we find $1/\kappa \approx 4$ nm. Assuming only monovalent ions in solution, this Debye length gives an ionic concentration for the solvent of about 6 mM [48]. For comparison, the Debye length and ionic concentration of neutral pH pure water are 960 nm and 10^{-4} mM. Therefore, the solutions contained non-negligible concentrations of dissolved ions, originating from surface dissociation on the particles and the incomplete removal of the NaOH stabilizer. These ions caused the particles to behave as hard spheres with an effective hard sphere radius greater than the actual particle radius.

Next, we consider the change in ϕ between the SAXS measurements made before freezing the samples and after melting. The particle volume fraction obtained after adjustment from the fitted ϕ_{HS} tended to drop from about 0.02 before freezing to around 0.01 after melting. This decrease indicates that after being frozen and melted, the bulk solution contained less than half as many particles as it contained before being frozen. The missing particles presumably sedimented as aggregates, as we observed in the direct imaging ex-

periments. Because the particles used in our experiments have a very small Peclet number (about 10^{-5}), Brownian motion is sufficient to keep individual particles suspended almost indefinitely. However, the increased mass of particle aggregates could cause sedimentation on experimentally relevant time scales [35]. Therefore, the SAXS results from the unfrozen samples imply that about half of the particles originally in the solution ended up in these aggregates and subsequently sedimented upon melting of the ice. The aggregates most likely formed in the high particle density regions created by rejection of particles from the ice dendrites. This is supported by the interpretation of the SAXS data collected while the samples were frozen.

The scattered intensity from frozen samples had two primary features associated with structure possessing two distinct primary length scales. The high scattering vector peak corresponds to the inter-particle spacing of colloids within the high density regions and the low scattering vector upturn is related to the size of the high density domains. If we could extend our measurements of the scattered intensity to lower scattering vectors, we would expect to find that the upturn is in fact a peak and its position would give the size of the high density domains (as in references [54–56]) or the spacing between them. In the present experiments, the minimum q gives a lower bound for the size of these features: $2\pi/q_{min} = 2\pi/0.02\ \text{nm}^{-1} = 314$ nm, or approximately 10 times the particle radius. Further measurements at lower scattering vectors would also help clarify the medium-scale structure of the high density regions, i.e., the arrangement of particles on length scales greater than that of a single particle, but still within a single high density region. Although the failure of the fractal cluster model to fit the low-q upturn in our data *suggests* that structure at this scale is not fractal, there are insufficient data to rule this out or to advance other possibilities.

On the other hand, the high scattering vector feature provides more reliable information because the full peak falls within our accessible q-range. This peak reflects how the particles packed as they were rejected during freezing. We can rule out a crystalline arrangement of the particles because the peak is too broad. We did not expect that the particles in the present experiments would pack this way due to their large polydispersity, which is known to inhibit colloidal crystallization [57]. In addition, colloidal crystallization is an equilibrium process requiring some amount of time to proceed. Although an ordered particle packing has been observed in at least one directional solidification experiment [4], the densification of the particles upon rejection during freezing in our samples was most likely too rapid to

permit this process [58]. Therefore, the particles in the high density regions packed in a predominantly amorphous or random arrangement.

Particles in an amorphous packing, like particles in a colloidal crystal, are characterized by an average inter-particle distance though the variation around this average distance is greater in amorphous packings than in crystalline ones. The position of the SAXS peak is approximately related to this distance by $2\pi/q_{peak}$, which gives an interparticle distance on the order of the particle diameter. Therefore, the particles in the high density regions were generally in contact with their nearest neighbors. However, as we cannot determine the particle volume fraction in this way, this is not a complete description of the structure. Knowing that on average particles were in contact with their nearest neighbors offers no information about how many nearest neighbors an average particle contacts, which is related to the particle volume fraction.

Typically the volume fraction is quantified through the model for $S(q)$. However, our measured structure factors did not conform to any of the structure factors based on common particle pair potentials, which implies that the particle configuration within the high-particle-density regions was different from those that occur in high density colloidal fluids (c.f. reference [37]), glasses (c.f. reference [28]), or gels (c.f. reference [59]) even though the underlying particle interactions are similar (long-range repulsive or hard sphere interactions and short-range attraction). In general, the peak in our data was broader and higher than that predicted by any of the standard models. This means that our samples tended to be more heterogeneous with respect to the inter-particle spacing and have a greater number of nearest neighbors than expected. This could be due in part to the relatively high polydispersity of our colloidal particles, but may also reflect particular aspects of the densification process that occurs during freezing.

Polydispersity is difficult to incorporate into models for $S(q)$ and is not included in any of the models generally used to fit scattering data, including all of those we investigated. Qualitatively however, polydisperse particles can have not only a broader range of inter-particle distances than comparable monodisperse particles, but also are known from simulations to pack more densely while still maintaining a mostly random arrangement [60–62], thereby allowing a greater number of nearest neighbors. Such effects are not included in the standard structure factors, but could produce structure factors with wider peaks located at higher scattering vectors. As an example of this, Pham and coworkers [63] suggested that a shift

in the peak position in their scattering data from $qR \approx 3.8$ to $qR \approx 4.0$ corresponded to a change in the local particle volume fraction from 0.60 to 0.69, the random close packing limit for their system. The enhancement above the often-quoted random close packing value of 0.64 was attributed to particle polydispersity. They did not fit their data to a model. Therefore, based on their empirical relation and the location of our peak at $qR \approx 3.94$, we estimate that the particles in the high density regions had a volume fraction near 0.66. This is similar to the predictions from simulations for spheres of similar polydispersity, which range from 0.66 to 0.68 [60, 61].

Alternately, the discrepancy between our SAXS data and the standard models may stem from the forcing of the particles by the growing ice (discussed below). Much work has been directed at studying the influence of external forcing on structure in various colloidal materials. The most commonly studied external forcing is that resulting from shear flow imposed on a sample in one of the various colloidal phases (e.g., references [64–66]). However, the structure investigated is usually on a scale many times the particle size and shear flow is not necessarily comparable to what occurs during freezing. In contrast, Kurita and Weeks [67] examined a layer of randomly close packed, sedimented particles using confocal microscopy and calculated a structure factor from the real-space positions of about $450,000$ particles. They found that the resulting $S(q)$ had a primary peak near $qR \approx 3.93$ (versus 3.94 for our system), but did not attempt to fit their structure factor to any models. Their system had an overall volume fraction of about 0.646 with small, locally ordered regions having ϕ up to about 0.68. Sedimentation involves a gradual increase in the particle density and compression of the colloidal fluid, similar to what happens during freezing when the growing solid continually squeezes the particles into the shrinking volume of unfrozen liquid. Therefore, we might expect that our samples had a structure with characteristics similar to that of the sedimented layer.

Finally, we note that the discrepancy could simply result from the failure of the standard models to describe colloidal solutions at such high densities. Although in many cases the various analytical structure factors have been found to agree reasonably well up to volume fractions near 0.6 (e.g., reference [68]), most were not intended to be applied for volume fractions above about 0.4. Most likely the discrepancy observed in our system resulted from some combination of all three factors: polydispersity, particle forcing, and model inadequacy at high ϕ. More experiments and theoretical work could help clarify these issues. Nonethe-

less, we can conclude that the present experiments reveal that the particles rejected from the ice dendrites are touching and likely close packed to near their jammed limit.

With this knowledge, we can explain the formation of the observed particle aggregates. Before the particles can aggregate though, they must be brought into contact. In order to bring the particles into contact, the ice must have exerted a force on the particles sufficient to overcome the repulsion between two particles resulting from the surface charges and double layer. This force is estimated from the Debye length and surface charge to be about 2.5×10^{-10} N [35]. If the force from the ice is assumed to have been distributed across half of one of the particles (with the other particle held fixed), then the pressure that the ice must have applied to the particle is about 3.5×10^4 Pa, or 0.34 atm. From frost heaving of soils the maximum overpressure at which heaving stops has been measured at about 11 atm per °C of cooling below T_m [7], so for the present experiments where freezing occurred below -20°C the pressure on the particles may have been larger than 200 atm. Thus, it is reasonable that the ice should be able to overcome the repulsive force between the particles and push them into close contact.

Once this repulsion was overcome and the particles were forced into contact by the ice dendrites, the attractive van der Waal's force should have dominated the interaction, allowing the particles to form aggregates. Using the Hamaker constant for fused quartz, the attraction potential between two particles is -9.4×10^{-20} J, or about $25 k_B T$ at $T = 0$°C, where k_B is Boltzmann's constant [48]. This is sufficient to maintain the aggregates' integrity well above the melting temperature. Alternatively, once the particles were forced into contact they may have fused together chemically or physically due to damage near the inter-particle contacts. In either case, this suggests that the aggregates were the direct result of particle rejection to the inter-dendrite regions during freezing. Combined with the SAXS results from the solutions when unfrozen, we can then estimate that at least half of the particles in the solution ended up in these high density regions. However, this is a lower bound, and in fact nearly all of the particles may have been caught between the dendrites, but some were individually engulfed by the ice or subsequently stripped from the aggregates by dynamic processes [43].

These observations have several implications for our understanding of directional solidification of colloidal suspensions. First, models based on the purely statistical mechanical behavior of colloidal *solutions*, while a reasonable and necessary starting point, are likely

not adequate to completely explain the phenomena observed during solidification. That is, the densification that occurs as the solutions freeze is not analogous to that resulting from simply increasing the density of particles in a colloidal fluid. Second, the results add experimental evidence to the common assumption that the colloidal particles close pack upon rejection from the solidification front and suggest that the packing achieved may be the densest possible amorphous packing that can be produced given the particles' distribution of sizes. Furthermore, the high particle density regions appear to be compact (i.e., not fractal) on the scale of several particle diameters. Finally, the observation of particle aggregates whose attractive van der Waal's interaction is sufficient to maintain their integrity after melting suggests the possibility of creating macroscopic freeze-cast materials without the need for special binding or sintering techniques.

In addition, our results may be useful in understanding other systems involving driven, high concentration colloidal suspensions. They suggest that the arrangement of particles at the smallest scales may not conform to predictions based solely on the interparticle interactions. Such differences could potentially influence the flow properties of the material or dynamic behavior of the particles, which are of interest scientifically and for engineering applications. However, more work is needed before the discrepancies between the measured and predicted structure factors can be unequivocally attributed to effects of the driving force. Further study of the structure factor could also incorporate hydrodynamic interactions between the particles and the effects of the driving force (such as repulsion from the ice), as has been done for the well characterized shear flow geometry [66]. Extending such work to more complicated forcing configurations and flow geometries is important because these types of situations are often encountered in practical applications. Overall, solidified colloidal suspensions are a promising system in which to study the effects of external driving on particle arrangement because the particle-scale structure is effectively "frozen in" both by the constraint of the surrounding ice and the strong van der Waal's attraction between the particles.

VI. CONCLUSION

We have presented a joint small angle X-ray scattering and direct imaging study of solidifying and frozen colloidal suspensions. Our results highlight the utility of these methods

for studying the structure of such materials and suggest routes for future investigation. By consulting the images acquired directly in laboratory freezing experiments, we identified the main peak exhibited by the scattered X-ray intensity from frozen solutions as resulting from the close packing of particles in high-particle-density regions formed between ice dendrites. The enhanced intensity at low scattering vectors we attributed to the size of the high density regions. In addition, the close packing of the particles produced by freezing allowed the short-range attractive inter-particle interaction to dominate thereby creating long-lived particle aggregates. However, we found that the structure observed in our samples when they were frozen could not be described by any of the standard inter-particle potentials even though the unfrozen solutions were well-described by a hard sphere interaction with an effective hard sphere radius. This implies that the process of freezing produces atypical arrangements of the colloidal particles.

Further work could help clarify some of the issues encountered and expand upon the present conclusions. Importantly, by altering the solidification conditions, more controlled freezing could be attained and particle structure (including volume fraction) ahead of a solidification front (planar or dendritic/cellular) could be studied. Examining samples with a variety of higher and lower initial volume fractions would help determine the robustness of the close packed arrangement. Similarly, using different sizes or types of particles would also contribute to answering this question. Different size particles would shift the qR range accessed by SAXS and hence the scale of the structures investigated with respect to the particle size. Different types of particles with a more monodisperse size distribution would interact differently with each other, possibly conforming more closely to one of the standard inter-particle potentials, which would either allow more accurate modelling of the frozen structure or confirm that the freezing process imposes a unique structure among the particles.

Finally, three other X-ray scattering techniques can provide complementary information about the samples and should be utilized for studying solidifying colloidal suspensions. First, dynamic X-ray scattering, or X-ray photon correlation spectroscopy (XPCS), allows for determination of how the particles are moving, such as distinguishing between diffusive and ballistic motion and measuring the rate of this motion. We have applied XPCS to examine particles in frozen samples during aging and present those results elsewhere [43]. A second technique is X-ray near field scattering (XNFS), which combines aspects of X-ray scattering and radiography, and also provides structural and dynamic information, though the analysis

of the data is more complicated than in SAXS or XPCS [69]. However, XNFS has the benefits of accessing smaller wavevectors than SAXS and permitting observation during freezing. Third, ultra-small angle X-ray scattering (USAXS) can also access smaller wavevectors, but with a data analysis procedure similar to that for standard SAXS [70]. USAXS could clarify the structure at intermediate length scales and possibly identify the length scale associated with the low-q intensity upturn seen in our experiments. By combining SAXS and other X-ray techniques future work will greatly increase our knowledge of the small scale structure resulting from solidification of colloidal suspensions, which in turn will help enhance understanding of the processes occurring during solidification and allow for better control of the final solidified product.

ACKNOWLEDGMENTS

We thank S. Narayanan, A. Sandy and M. Sprung for assistance with the SAXS experiments, and X. Lu, J. Neufeld, E. Thomson and L. Wilen for useful discussions. MS acknowledges the National Science Foundation (NSF) Graduate Research Fellowship Program for support. SGJM thanks the NSF for support via DMR-0906697. SSLP acknowledges support from the King Abdullah University of Science and Technology (KAUST), Award No. KUK-C1-013-04. JSW acknowledges support from the NSF Grant No. OPP0440841 and the US Department of Energy Grant No. DE-FG02-05ER15741. Use of the Advanced Photon Source at Argonne National Laboratory was supported by the US Department of Energy, Office of Science, Office of Basic Energy Sciences, under Contract No. DE-AC02-06CH11357.

---

[1] S. Deville, Adv. Eng. Mater, **10**, 155 (2008).

[2] Q. Fu, M. N. Rahaman, F. Dogan, and B. S. Bal, J. Biomed. Mater. Res. A, **86B**, 125 (2008).

[3] S. Deville, E. Saiz, R. K. Nalla, and A. P. Tomsia, Science, **311**, 515 (2006).

[4] J.-W. Kim, K. Tazumi, R. Okaji, and M. Ohshima, Chem. Mater., **21**, 3476 (2009).

[5] G. Wilde and J. H. Perepezko, Mat. Sci. Eng. A - Struct., **283**, 25 (2000).

[6] G. Gay and M. A. Azouni, Cryst. Growth Des., **2**, 135 (2002).

[7] J. G. Dash, A. W. Rempel, and J. S. Wettlaufer, Rev. Mod. Phys., **78**, 695 (2006).

[8] D. R. Uhlmann and B. Chalmers, J. Appl. Phys., **35**, 2986 (1964).

[9] M. A. Azouni, W. Kalita, and M. Yemmou, J. Cryst. Growth, **99**, 201 (1990).

[10] A. W. Rempel and M. G. Worster, J. Cryst. Growth, **205**, 427 (1999).

[11] S. S. L. Peppin, M. G. Worster, and J. S. Wettlaufer, Proc. R. Soc. A, **463**, 723 (2007).

[12] S. Taber, J. Geol., **37**, 428 (1929).

[13] K. Watanabe and M. Mizoguchi, J. Cryst. Gr., **213**, 135 (2000).

[14] H. Zhang, I. Hussain, M. Brust, M. F. Butler, S. P. Rannard, and A. I. Cooper, Nat. Mater., **4**, 787 (2005).

[15] S. S. L. Peppin, J. S. Wettlaufer, and M. G. Worster, Phys. Rev. Lett., **100**, 238301 (2008).

[16] S. Deville, E. Maire, G. Bernard-Granger, A. Lasalle, A. Bogner, C. Gauthier, J. Leloup, and C. Guizard, Nat. Mater., **8**, 966 (2009).

[17] S. S. L. Peppin, M. J. Spannuth, and J. S. Wettlaufer, J. Stat. Phys., **134**, 701 (2009).

[18] C. Allain and L. Limat, Phys. Rev. Lett., **74**, 2981 (1995).

[19] M. D. Haw, Phys. Rev. Lett., **92**, 185506 (2004).

[20] A. I. Campbell and M. D. Haw, Soft Matter, **6**, 4688 (2010).

[21] N. O. Shanti, K. Araki, and J. W. Halloran, J. Am. Ceram. Soc., **89**, 2444 (2006).

[22] T. Waschkies, R. Oberacker, and M. J. Hoffmann, J. Am. Ceram. Soc., **92**, S79 (2009).

[23] S. Deville, E. Maire, A. Lasalle, A. Bogner, C. Gauthier, J. Leloup, and C. Guizard, J. Am. Ceram. Soc., **92**, 2489 (2009).

[24] J. A. Sekhar and R. Trivedi, Mat. Sci. Eng. A - Struct., **47**, 9 (1991).

[25] T. Weitkamp, P. Tafforeau, E. Boller, P. Cloetens, J. Valade, P. Bernard, F. Peyrin, W. Ludwig, L. Helfen, and J. Baruchel, Proc. X-ray Optics and Microanalysis, **1221**, 33 (2010).

[26] L. B. Lurio, D. Lumma, A. R. Sandy, M. A. Borthwick, P. Falus, S. G. J. Mochrie, J. F. Pelletier, M. Sutton, L. Regan, A. Malik, and G. B. Stephenson, Phys. Rev. Lett., **84**, 785 (2000).

[27] J. Wagner, T. Autenrieth, A. Robert, W. Härtl, and G. Grübel, J. Magn. Magn. Mat., **289**, 54 (2005).

[28] X. Lu, S. G. J. Mochrie, S. Narayanan, A. R. Sandy, and M. Sprung, Phys. Rev. Lett., **100**, 045701 (2008).

[29] P. N. Pusey, in *Neutrons, X-rays and Light: Scattering Methods Applied to Soft Condensed Matter*, edited by P. Linder and T. Zemb (North-Holland, 2002) Chap. 1, pp. 3–21.

[30] B. J. Berne and R. Pecora, *Dynamic Light Scattering* (John Wiley and Sons, 1976).

[31] J. S. Pedersen, in *Neutrons, X-rays and Light: Scattering Methods Applied to Soft Condensed Matter*, edited by P. Linder and T. Zemb (North-Holland, 2002) Chap. 16, pp. 391–420.

[32] R. Klein, in *Neutrons, X-rays and Light: Scattering Methods Applied to Soft Condensed Matter*, edited by P. Linder and T. Zemb (North-Holland, 2002) Chap. 14, pp. 351–379.

[33] H. Wiese and D. Horn, J. Chem. Phys., **94**, 6429 (1991).

[34] W. W. Mullins and R. F. Sekerka, J. Appl. Phys., **35**, 444 (1964).

[35] M. Spannuth, *Structure and Dynamics in Freezing and Frozen Colloidal Suspensions from Direct Imaging and X-ray Scattering*, PhD Thesis, Geophysics, Yale University (2010).

[36] L. A. Wilen and J. G. Dash, Phys. Rev. Lett., **74**, 5076 (1995).

[37] D. Lumma, L. B. Lurio, M. A. Borthwick, P. Falus, and S. G. J. Mochrie, Phys. Rev. E, **62**, 8258 (2000).

[38] P. Falus, M. A. Borthwick, and S. G. J. Mochrie, Rev. Sci. Instrum., **75**, 4383 (2004).

[39] S. Schöder, H. Reichert, H. Schröder, M. Mezger, J. S. Okasinski, V. Honkimäki, J. Bilgram, and H. Dosch, Phys. Rev. Lett., **103**, 095502 (2009).

[40] W. W. Mullins and R. F. Sekerka, J. Appl. Phys., **34**, 323 (1963).

[41] A. A. Shibkov, Y. I. Golovin, M. A. Zheltov, A. A. Korolev, and A. A. Leonev, Physica A, **319**, 65 (2003).

[42] T. Ishizaki, M. Maruyama, Y. Furukawa, and J. G. Dash, J. Cryst. Growth, **163**, 455 (1996).

[43] M. J. Spannuth, S. G. J. Mochrie, S. S. L. Peppin, and J. S. Wettlaufer, In preparation (2010).

[44] S. R. Aragón and R. Pecora, J. Chem. Phys., **64**, 2395 (1976).

[45] K. Dawson, G. Foffi, M. Fuchs, W. Götze, F. Sciortino, M. Sperl, P. Tartaglia, T. Voigtmann, and E. Zaccarelli, Phys. Rev. E, **63**, 011401 (2000).

[46] D. Pontoni, T. Narayanan, J. Petit, G. Grübel, and D. Beysens, Phys. Rev. Lett., **90**, 188301 (2003).

[47] J. B. Hayter and J. Penfold, Mol. Phys., **42**, 109 (1981).

[48] J. Israelachvili, *Intermolecular and Surface Forces*, 2nd ed. (Academic Press, 1992).

[49] W. O. Roberts, *Colloidal Silica: Fundamentals and Applications* (Taylor and Francis, 2006).

[50] A. P. Philipse and A. Vrij, J. Chem. Phys., **88**, 6459 (1988).

[51] A. P. Philipse and A. Vrij, J. Colloid Interf. Sci., **128**, 121 (1989).

[52] A. Imhof, A. van Blaaderen, G. Maret, J. Mellema, and J. K. G. Dhont, J. Chem. Phys., **100**, 2170 (1994).

[53] G. Nägele, M. Watzlawek, and R. Klein, Progr. Colloid Polym. Sci., **104**, 31 (1997).

[54] A. Stradner, H. Sedgwick, F. Cardinaux, W. C. K. Poon, S. U. Egelhaaf, and P. Schurtenberger, Nature, **432**, 492 (2004).

[55] M. Lattuada, H. Wu, and M. Morbidelli, Langmuir, **20**, 4355 (2004).

[56] F. Sciortino, S. Mossa, E. Zaccarelli, and P. Tartaglia, Phys. Rev. E, **69**, 011503 (2004).

[57] S. Auer and D. Frenkel, Nature, **413**, 711 (2001).

[58] S. Auer and D. Frenkel, Nature, **409**, 1020 (2001).

[59] S. A. Shah, Y.-L. Chen, S. Ramakrishnan, K. S. Schweizer, and C. F. Zukoski, J. Phys.: Condens. Matter, **15**, 4751 (2003).

[60] W. Schaertl and H. Sillescu, J. Stat. Phys., **77**, 1007 (1994).

[61] R. S. Farr and R. D. Groot, J. Chem. Phys., **131**, 244104 (2009).

[62] M. Hermes and M. Dijkstra, Europhys. Lett., **89**, 38005 (2010).

[63] K. N. Pham, S. U. Egelhaaf, P. N. Pusey, and W. C. K. Poon, Phys. Rev. E, **69**, 011503 (2004).

[64] M. D. Haw, W. C. K. Poon, and P. N. Pusey, Phys. Rev. E, **57**, 6859 (1998).

[65] P. Varadan and M. J. Solomon, Langmuir, **17**, 2918 (2001).

[66] J. Vermant and M. J. Solomon, J. Phys.: Condens. Matter, **17**, R187 (2005).

[67] R. Kurita and E. R. Weeks, Phys. Rev. E, **82**, 011403 (2010).

[68] P. N. Pusey and W. van Megen, Phys. Rev. Lett., **59**, 2083 (1987).

[69] R. Cerbino, L. Peverini, M. A. C. Potenza, A. Robert, P. Bösecke, and M. Giglio, Nat. Phys., **4**, 238 (2008).

[70] M. Morvan, D. Espinat, J. Lambard, and T. Zemb, Colloid Surface A, **82**, 193 (1994).

RECENT REPORTS

35/10	Regularized Particle Filter with Langevin Resampling Step	Duan Farmer Moroz
36/10	Sequential Inverse Problems Bayesian Principles and the Logistic Map Example	Duan Farmer Moroz
37/10	Circumferential buckling instability of a growing cylindrical tube	Moulton Goriely
38/10	Preconditioners for state constrained optimal control problems with Moreau-Yosida penalty function	Stoll Wathen
39/10	Local synaptic signaling enhances the stochastic transport of motor-driven cargo in neurons	Newby Bressloff
40/10	Convection and Heat Transfer in Layered Sloping Warm-Water Aquifer	McKibbin Hale Style Walters
41/10	Optimal Error Estimates of a Mixed Finite Element Method for Parabolic Integro-Differential Equations with Non Smooth Initial Data	Goswami Pani Yadav
42/10	On the Linear Stability of the Fifth-Order WENO Discretization	Motamed Macdonald Ruuth
43/10	Four Bugs on a Rectangle	Chapman Lottes Trefethen
44/10	Mud peeling and horizontal crack formation in drying clay	Style Peppin Cocks
45/10	Binocular Rivalry in a Competitive Neural Network with Synaptic Depression	Kilpatrick Bressloff
46/10	A theory for the alignment of cortical feature maps during development	Bressloff Oster
47/10	All-at-Once Solution if Time-Dependent PDE-Constrained Optimisation Problmes	Stoll Wathen
48/10	Possible role of differential growth in airway wall remodeling in asthma	Moulton Goriely
49/10	Variational Data Assimilation Using Targetted Random Walks	Cotter Dashti Robinson Stuart

50/10	A model for the anisotropic response of fibrous soft tissues using six discrete fibre bundles	Flynn Rubin Nielsen
51/10	STOCHSIMGPU Parallel stochastic simulation for the Systems Biology Toolbox 2 for MATLAB	Klingbeil Erban Giles Maini
52/10	Order parameters in the Landau-de Gennes theory - the static and dynamic scenarios	Majumdar
53/10	Liquid Crystal Theory and Modelling Discussion Meeting	Majumdar Mottram
54/10	Modeling the growth of multicellular cancer spheroids in a bioengineered 3D microenvironment and their treatment with an anticancer drug	Loessner Flegg Byrne Hall Moroney Clements Hutmacher McElwain
55/10	Scalar Z, ZK, KZK, and KP equations for shear waves in incompressible solids	Destrade Goriely Saccomandi
56/10	The Influence of Bioreactor Geometry and the Mechanical Environment on Engineered Tissues	Osborne ODea Whiteley Byrne Waters
57/10	A numerical guide to the solution of the bidomain equations of cardiac electrophysiology	Pathmanathan Bernabeu Bordas Cooper Garny Pitt-Francis Whiteley Gavaghan

Copies of these, and any other OCCAM reports can be obtained from:

Oxford Centre for Collaborative Applied Mathematics
Mathematical Institute
24 - 29 St Giles'
Oxford

OX1 3LB
England
www.maths.ox.ac.uk/occam